Revealing the effects of laser beam shaping on melt pool behaviour in conduction-mode laser melting

Ebrahimi, Amin; Sattari, Mohammad; Babu, Aravind; Sood, Arjun; Römer, Gert Willem R.B.E.; Hermans, Marcel J.M.

DOI
10.1016/j.jmrt.2023.11.046

Publication date
2023

Document Version
Final published version

Published in
Journal of Materials Research and Technology

Journal of Materials Research and Technology 27 (2023) 3955–3967

Contents lists available at ScienceDirect

Journal of Materials Research and Technology

journal homepage: www.elsevier.com/locate/jmrt

Revealing the effects of laser beam shaping on melt pool behaviour in conduction-mode laser melting

Amin Ebrahimi [a,*], Mohammad Sattari [b], Aravind Babu [a], Arjun Sood [a], Gert-Willem R.B.E. Römer [b], Marcel J.M. Hermans [a]

[a] Department of Materials Science and Engineering, Faculty of Mechanical, Maritime and Materials Engineering, Delft University of Technology, Mekelweg 2, 2628CD Delft, The Netherlands

[b] Chair of Laser Processing, Department of Mechanics of Solids, Surfaces and Systems (MS^3), Faculty of Engineering Technology, University of Twente, Drienerlolaan 5, 7522NB Enschede, The Netherlands

ARTICLE INFO

Keywords:
Fusion welding and additive manufacturing
Laser beam shaping
Melt pool behaviour
Microstructural grain morphology
Bead profile
High-fidelity numerical simulation

ABSTRACT

Laser beam shaping offers remarkable possibilities to control and optimise process stability and tailor material properties and structure in laser-based welding and additive manufacturing. However, little is known about the influence of laser beam shaping on the complex melt-pool behaviour, solidified melt-track bead profile and microstructural grain morphology in laser material processing. A simulation-based approach is utilised in the present work to study the effects of laser beam intensity profile and angle of incidence on the melt-pool behaviour in conduction-mode laser melting of stainless steel 316L plates. The present high-fidelity physics-based computational model accounts for crucial physical phenomena in laser material processing such as complex laser–matter interaction, solidification and melting, heat and fluid flow dynamics, and free-surface oscillations. Experiments were carried out using different laser beam shapes and the validity of the numerical predictions is demonstrated. The results indicate that for identical processing parameters, reshaping the laser beam leads to notable changes in the thermal and fluid flow fields in the melt pool, affecting the melt-track bead profile and solidification microstructure. The columnar-to-equiaxed transition is discussed for different laser-intensity profiles.

1. Introduction

Laser beam melting offers unique controllability and high spatial and temporal precision in manufacturing high-integrity metallic products and has been utilised in many industries [1]. Melting and solidification in laser welding and additive manufacturing considerably affect local microstructural features (*i.e.* solidification morphology, grain size and crystallographic texture) [2–5] and the macroscale structure and properties of the material [6–8]. Studies have demonstrated that internal flow behaviour in melt pools has a significant influence on melting and subsequent solidification [9,10], hence it needs to be controlled effectively to achieve the desired properties [11]. However, controlling internal flow behaviour in laser welding and additive manufacturing is challenging mainly due to the complexity of molten metal flow dynamics and high sensitivity to changes in process parameters [12–14]. Therefore, understanding underlying physical phenomena in laser melting (*i.e.* laser–matter interaction, heat and molten metal flow, and solid–liquid phase transformation) is crucial for effective control of the melt-pool behaviour.

Previous studies suggest laser intensity profile as a critical factor influencing the processing window, melt-pool shape and dimension, and product quality in laser welding and additive manufacturing [15–19]. Changes in the laser intensity profile in such processes affect heating and cooling cycles by influencing convection in the melt pool [20] and hence can lead to changes in thermal gradients and solidification growth rates [21–23]. Advancements in optics and laser technology have opened up new possibilities for modulating spatial and temporal laser intensity profiles with high resolution, which is beneficial to enhancing process stability and control in laser material processing. Various techniques have been developed to tailor laser beam shape, which are reviewed comprehensively elsewhere [24,25]. However, the influence of tuning spatial laser intensity profile (commonly known as laser beam shaping) on internal flow behaviour has been overlooked and only sparsely investigated, particularly concerning conduction-mode laser melting, which serves as the foundation for numerous welding and additive manufacturing techniques. Moreover, the design and optimisation of laser intensity profile usually relies on trial-and-error

* Corresponding author.
E-mail address: A.Ebrahimi@tudelft.nl (A. Ebrahimi).

https://doi.org/10.1016/j.jmrt.2023.11.046
Received 22 September 2023; Accepted 6 November 2023
Available online 8 November 2023

experiments that are generally expensive and time-consuming [26,27]. This highlights the necessity of developing reliable predictive models that facilitate design-space exploration and process optimisation within a reasonable timeframe.

Studies on the effect of laser beam shaping in fusion welding and additive manufacturing, to a great extent, are experimental and focus primarily on measuring melt-pool shape and the resulting solidification texture and microstructural properties (see for instance [2,15,18,28,29]). High-fidelity numerical simulations supplement experimental studies by providing a better insight into the complex heat and fluid flow in melt pools and associated melting and solidification, supporting the development of process design and optimisation for laser-based manufacturing. Han and Liou [30] developed a three-dimensional computational model and studied the effects of employing a rectangular and three different axisymmetric laser intensity profiles on the evolution of thermal and fluid flow fields in stationary laser melting of a stainless steel alloy (AISI 304). In their model, Han and Liou [30] neglected the influence of surface-active elements on Marangoni flow pattern. Safdar et al. [31] conducted three-dimensional numerical simulations to study the effects of different rectangular beam shapes on thermal and fluid flow fields in laser melting of a mild steel alloy (EN-43 A). They neglected the influence of surface-active elements on the Marangoni flow pattern in their model and assumed that the melt-pool surface is flat and does not deform during the process. Numerical predictions of laser beam welding of aluminium-copper alloys reported by Rasch et al. [32] showed that the average surface temperature and resulting recoil pressure changes notably when using different beam shapes with comparable laser powers. Roehling et al. [3,4] studied the effects of elliptical laser beam shapes on the resulting microstructure of stainless steel 316L in laser powder-bed additive manufacturing and demonstrated experimentally that microstructure grain nucleation and morphology could be controlled using the laser beam shaping technique. Later, Shi et al. [5] developed a cellular automaton model to predict solidification grain structure using elliptical laser beam shapes in laser powder-bed additive manufacturing and employed a thermal-fluid model to predict the evolution of the thermal field during the process. The influence of surface-active elements on Marangoni flow pattern was neglected in their thermal-fluid simulations. Focusing on conduction-mode laser melting of Ti6Al4V alloy, Abadi et al. [33] numerically studied the effects of using elliptical and circular beams with a Gaussian intensity profile on molten metal flow behaviour and melt-pool shape. In these studies, the effects of surface morphology, laser incidence angle and temperature on local energy absorption are neglected and the value of absorptivity is assumed to be constant. Neglecting these factors limits the general applicability of the model in predicting melt-pool behaviour for different laser intensity profiles and various laser material processing scenarios. Despite the great potential of laser beam shaping for improving process control and final product quality, very little is known about the influence of various laser beam shapes on heat and fluid flow in melt pools and the resulting bead quality.

The present work focuses on studying laser beam melting of metallic substrates using different beam shapes, intensity profiles and laser beam incidence angles. The analysis primarily concentrates on conduction-mode laser melting, which forms the basis for a wide variety of welding and additive manufacturing techniques. Due to highly transient and complex molten metal flow behaviour, involving multiple physical effects such as solid–liquid phase transformation, laser-material interactions and free-surface oscillations, it is challenging to investigate the evolution of melt-pool behaviour using merely trial-and-error experiments. In the present work, high-fidelity three-dimensional numerical simulations are performed to describe geometrical evolution and molten metal flow dynamics of the melt pool. An enhanced laser absorptivity model [13] is utilised that takes into account the effects of surface morphology, material composition and surface temperature on local energy absorption. The model has been rigorously validated with experimental data acquired using various laser beam shapes. Subsequently, the validated model is employed to predict the effects of different laser intensity profiles on the melt-pool behaviour and resulting solidification microstructure. The present work offers a simulation-based approach to predict the effects of laser beam shaping in conduction-mode laser melting and to explore the design space for process optimisation at a reduced cost compared to experiments.

2. Methods

Three-dimensional physics-based numerical simulations were performed to study different beam shapes, intensity profiles and laser beam incidence angles in conduction-mode laser melting. The geometrical configuration of the problem, defined in a Cartesian coordinate system, together with the prescribed boundary conditions and the beam shapes studied in the present work are shown schematically in Fig. 1. For beam shapes shown in Fig. 1(b), a uniform intensity profile was employed. Beam shapes shown in Fig. 1(c) were produced by changing the laser beam incidence angle about the x or y axes, and the beam had a (pseudo-)Gaussian intensity profile. An Yb:YAG laser with an emission wavelength (λ) of 1.030×10^{-6} m, a laser power ($\mathscr{P}$) of 700 W and a focal spot diameter (d_b) of 1.5×10^{-3} m provides the thermal energy flux required to locally melt the plate that is made of stainless steel AISI 316L and is initially at room temperature ($T_i = 300$ K). The laser beam scans the surface at a fixed travel speed ($\mathscr{V}$) of 1.5×10^{-2} m s^{-1}, unless stated otherwise. To protect the molten material from oxidation, an argon shielding gas was employed.

The computational model was developed based on the finite-volume approach using a proprietary general-purpose solver, ANSYS Fluent [34]. The volume-of-fluid (VOF) method [35] was employed to model the movement of metal–gas interface. Details of the computational model are explained in our previous works [12,13,36,37], and are not repeated here. In the present work, temperature-dependent material properties are employed for AISI 316L, and the values are taken from [13]. The present model predicts multiple strongly-coupled physical processes that occur simultaneously during laser melting, such as variable laser absorptivity, molten metal flow due to Marangoni and thermal buoyancy forces, solid–liquid phase transformation and melt-pool surface deformation caused by the violent internal flow and the recoil pressure of metal vaporisation. Thermal and fluid flow fields and associated melt-pool surface movements were predicted by solving the conservation equations of mass, momentum, energy and a scalar field, called volume fraction ϕ to capture the position of the melt-pool surface, assuming that both the molten metal and argon are Newtonian fluids and that their densities are independent of any pressure variations that occur during processing. These are defined as follows:

$$\frac{D\rho}{Dt} + \rho(\nabla \cdot \mathbf{u}) = 0, \tag{1}$$

$$\rho\frac{D\mathbf{u}}{Dt} = \mu\nabla^2\mathbf{u} - \nabla p - C\,\frac{(1-\psi)^2}{\psi^3+\epsilon}\,\mathbf{u} + \mathbf{F}_s, \tag{2}$$

$$\rho\frac{Dh}{Dt} = \frac{k}{c_p}\nabla^2 h - \rho\frac{D\left(\psi\mathcal{L}_f\right)}{Dt} + S_q + S_l, \tag{3}$$

$$\frac{D\phi}{Dt} = 0. \tag{4}$$

Here, ρ is the density, $\mathbf{u}$ the fluid velocity vector, t the time, μ the dynamic viscosity, p the pressure, C the mushy-zone constant, equal to 10^7 kg m^{-2} s^{-2} [38], ϵ a constant incorporated to avoid division by zero, equal to 10^{-3}, h the sensible heat, k the thermal conductivity, c_p the specific heat capacity, $\mathcal{L}_f$ the latent heat of fusion, ψ the local liquid volume-fraction, and $(\psi\mathcal{L}_f)$ the latent heat of the material. The value of ϕ in a computational cell ranges between 0 and 1, representing the volume-fraction of the metal phase. Marangoni shear force, capillary force and recoil pressure are modelled by incorporating the source term $\mathbf{F}_s$ into the momentum equation (Eq. (2)) [13]. The energy input from the laser beam and heat losses from the workpiece

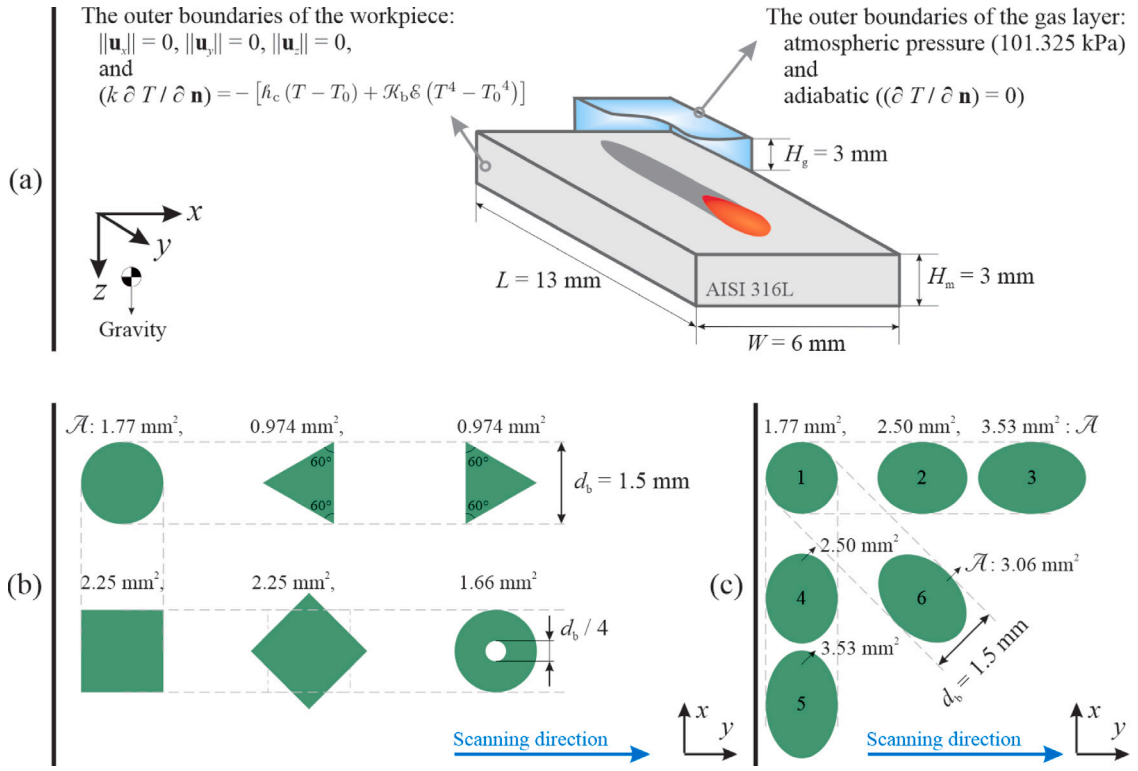

Fig. 1. (a) Schematic of laser beam melting, plate dimensions and the boundary conditions prescribed in numerical simulations. (b) different beam shapes with uniform intensity profile (the laser beam is perpendicular to the x-y plane), and (c) different beam shapes obtained by inclining the laser beam with (pseudo-)Gaussian intensity profile. Values shown above each laser beam shape indicate the area of laser focal spot $\mathcal{A}$.

due to convection, radiation and vaporisation are modelled by adding the source term S_q and the sink term S_l to the energy equation (Eq. (3)) respectively [12,13]. The boundary conditions prescribed at the outer boundaries of the computational domain are shown in Fig. 1. Spatial and temporal variations of the laser absorptivity during the process resulting from changes in surface temperature and laser beam incidence angle were modelled using an enhanced absorption model that is described in our previous work [13]. User-defined functions (UDFs) were employed to implement the source and sink terms in the governing equations, the laser absorptivity and surface tension models. The accuracy of the present computational model in predicting thermal profile and molten metal flow dynamics in laser melting is thoroughly investigated in our previous works [12,13,36,37] by comparing the numerical results with experimental and theoretical data for different laser systems and various laser beam intensity profiles and shapes. The validity of the model is further investigated in the present work, and the results are presented in Section 3.1.

The computational mesh consists of about 2×10^6 non-uniform hexahedral cells with minimum cell spacing of 4×10^{-5} m close to the gas–metal interface. The computational cell spacing was chosen sufficiently fine to achieve at least 35 cells along the melt-pool width, which is sufficient to obtain grid-independent numerical predictions [12,13,37]. The second-order central differencing scheme and the first-order implicit formulation were employed for spatial and temporal discretisation respectively. An explicit VOF method [39] was employed to capture the gas–metal interface. The PISO (pressure-implicit with splitting of operators) scheme [40] was employed for resolving the pressure–velocity coupling, and the PRESTO (pressure staggering option) scheme [41] was applied for the pressure interpolation. To keep the value of the Courant number ($\mathrm{Co} = \|\mathbf{u}\|\Delta t/\Delta x$) less than 0.25, a fixed time-step size of $\Delta t = 1 \times 10^{-6}$ s was employed.

The effects of laser beam shaping on microstructural grain structure are studied by computing the values of solidification growth rate (R) and thermal gradient (G) at the computational grid points located in the solidifying region (*i.e.* mushy region) as follows [5]:

$$G = \|\nabla T\| = \sqrt{\nabla T \cdot \nabla T}, \tag{5}$$

$$R = \mathcal{V} \cdot \cos(\alpha). \tag{6}$$

Here, α is the angle between the maximum heat flow direction and the scanning direction, and is determined as follows:

$$\alpha = \arccos\left(\frac{\partial T/\partial y}{G}\right). \tag{7}$$

The values of solidification growth rate (R) and thermal gradient (G) obtained from the simulations are plotted in the so-called 'solidification map'. The solidification map is divided into three regions according to the analytical model proposed by Hunt [42], indicating the nucleation propensity of fully columnar (characterised by high G/R values), fully equiaxed (characterised by low G/R values) and mixed columnar-equiaxed grains. According to the Hunt's model, the critical gradient conditions for fully columnar and fully equiaxed grain growth can be approximated respectively by

$$G > \xi\,\Delta T_c \sqrt[3]{100 \cdot N_0}\left(1 - \left(\frac{\Delta T_N}{\Delta T_c}\right)^3\right), \tag{8}$$

and

$$G < \xi\,\Delta T_c \sqrt[3]{N_0}\left(1 - \left(\frac{\Delta T_N}{\Delta T_c}\right)^3\right), \tag{9}$$

where, ξ is a constant equal to 0.617 [42], ΔT_c the undercooling for dendrite formation, N_0 the nucleation density and ΔT_N the critical undercooling for nucleation. Assuming that the tip velocity of the dendrite is equal to the solidification growth rate R [43], the undercooling for dendrite formation is determined by an empirical correlation as follows [5,44]:

$$\Delta T_c = \left(\frac{R}{a}\right)^{1/b}, \tag{10}$$

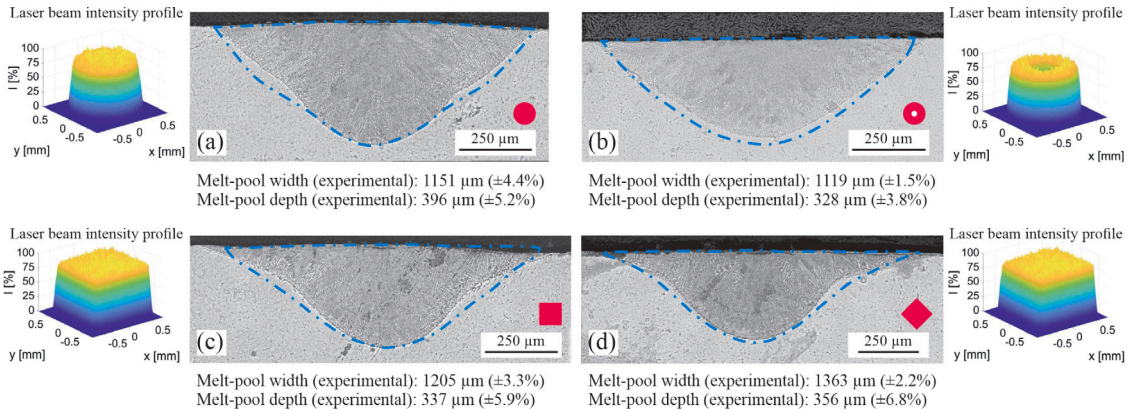

Fig. 2. Comparison of the numerically predicted melt-pool shapes using the present computational model with the experimental measurements for (a) circular, (b) annular, (c) square and (d) diamond laser beam shapes. Red symbols on each subfigure show the laser beam shape. Blue curves show the numerically predicted melt-pool shape. (For interpretation of the references to colour in this figure legend, the reader is referred to the web version of this article.)

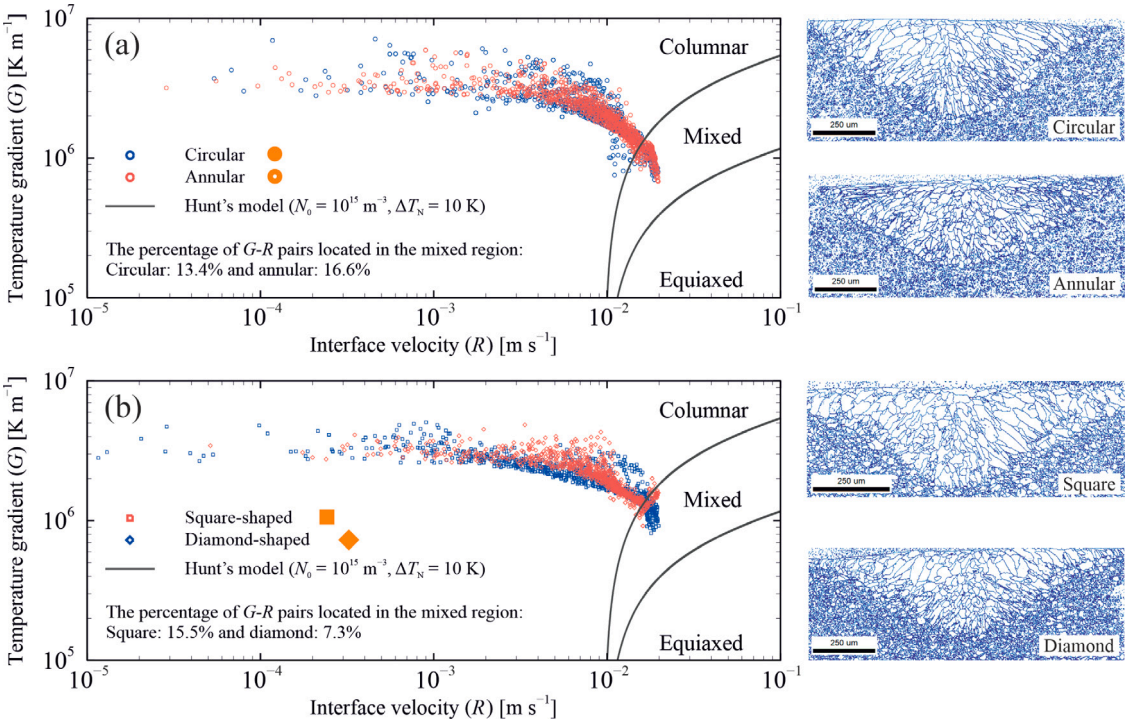

Fig. 3. The distribution of numerically predicted grain morphologies on the solidification map based on Hunt's model (left column) and the EBSD measurements (right column) for different laser beam shapes. Orange symbols show the laser beam shape.

where, a and b are constants whose values depend on the material and are equal to 7.325×10^{-6} and 3.12 respectively [45] for the alloy employed in the present study. The values of nucleation density N_0 and the critical undercooling for nucleation ΔT_N are taken from the literature [4,5,17] for stainless steel AISI 316L and are equal to 10^{15} m^{-3} and 10 K respectively.

3. Results and discussion

3.1. Model validation

Four different laser beam shapes were studied to examine the validity of the present numerical simulations in predicting the melt-pool shape and dimensions. An Yb:YAG laser (Trumpf TruDisk 10001) with an emission wavelength of $\lambda = 1.030 \times 10^{-6}$ m in combination with three optical transport fibres (*i.e.* a 600 μm circular core fibre, a 620 μm square core fibre and a 400/100 μm 2-in-1 core fibre) was employed in the experiments. The focusing optics (BEO D70 Trumpf) consist of a collimator with a focal length of 2×10^{-1} m and lenses with two different focal lengths of 4×10^{-1} m and 6×10^{-1} m. Employing the lens with a focal length of 6×10^{-1} m in combination with the 2-in-1 fibre, a beam with a focal spot size of $d_b = 1.2 \times 10^{-3}$ m and a uniform intensity profile in the focal plane, as shown in Fig. 2, was produced. The laser power ($\mathscr{P}$) was set to 500 W to locally melt a stainless steel AISI 316L plate at a fixed travel speed of $\mathscr{V} = 2 \times 10^{-2}$ m s^{-1}. The plate employed in the experiments had a cuboid shape with dimensions (x, y, z) of $100 \times 250 \times 10$ mm^3. Each experimental trial was conducted with a minimum of three repetitions to establish the replicability of the outcomes. To capture the experimental melt-pool shapes, macrographs were extracted *ex-situ* from middle of the melting track and photographed using a digital microscope. Uncertainties in experimental measurements of the melt-pool depth and width are about 4–7% and 2–4% respectively. Iso-surfaces of solidus temperature (T_s = 1658 K) obtained from the numerical simulations were used to visualise

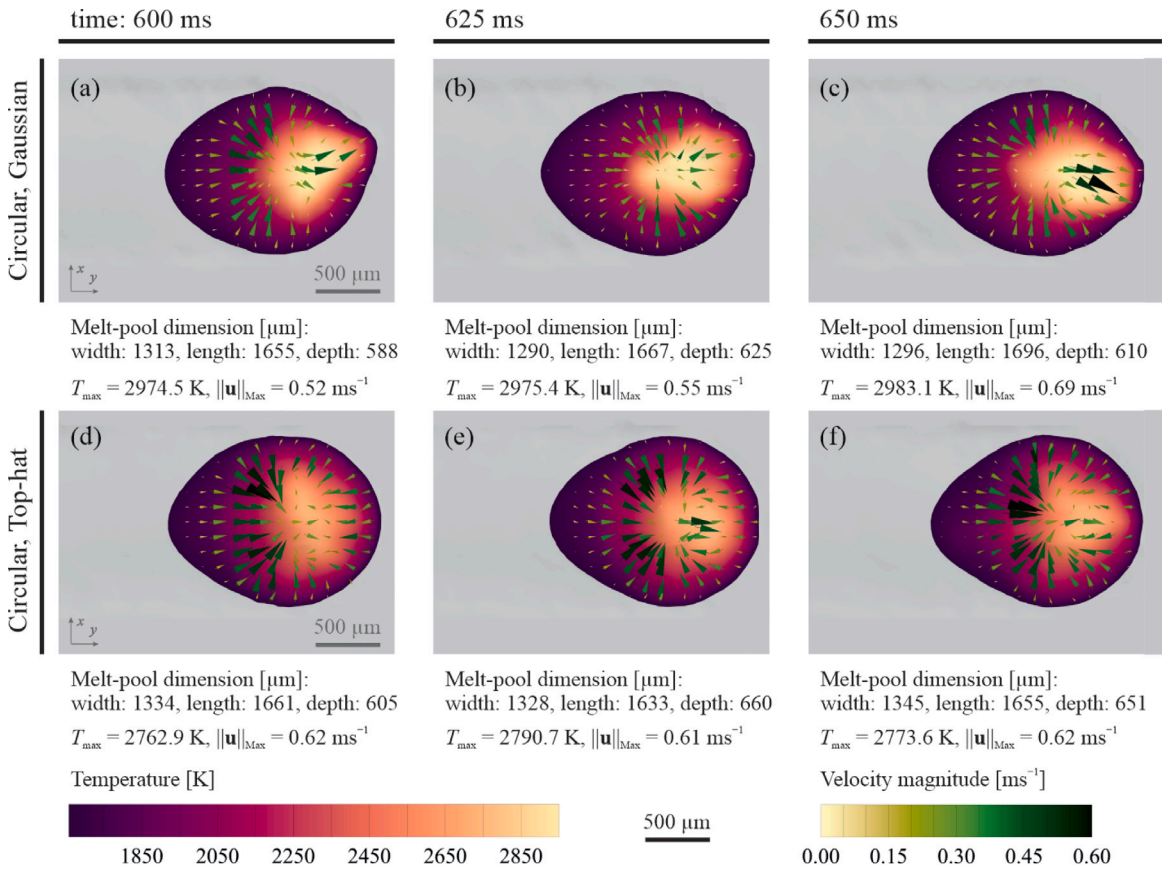

Fig. 4. Snapshots of thermal and fluid flow fields over the melt-pool surface at three different time instances and the predicted melt-pool dimensions for circular laser beams with Gaussian (a-c) and top-hat (d-f) intensity profiles. The laser power is 700 W and the travel speed is 1.5×10^{-2} m s^{-1}. The laser beam is perpendicular to the plate surface.

the melt-pool shape. A comparison is made between the numerically predicted and experimentally measured melt-pool shapes for different beams, and the results are shown in Fig. 2. The maximum absolute error in the prediction of melt-pool depth and width are less than 7% and 5% respectively, demonstrating a reasonable agreement without exercising any parameter tuning. Such an error is attributed to the simplifying assumptions made to develop the model, uncertainties associated with modelling material properties at elevated temperatures and experimental variations.

The numerically predicted *G*-*R* pairs for different laser beam shapes are plotted in the solidification map, as shown in Fig. 3. The solidification map is divided into three regions according to the analytical model proposed by Hunt [42]. EBSD (electron backscatter diffraction) technique was used to visualise microstructural grain structure on the transverse cross-sections of the melting track after the experiments, and the results are shown in Fig. 3. For EBSD measurements, the samples were further polished with colloidal silica for 50 minutes. A Thermo Scientific Helios G4 PFIB UXe SEM equipped with an EDAX detector was employed for EBSD analysis. A specimen tilt angle of 60° along with an accelerating voltage of 20 kV and a current of 3.2 nA was used for data acquisition. A step size of 0.8 μm was employed for the measurements. EBSD data processing was performed using EDAX OIM Analysis 8 software. The examination of EBSD data shows that changes in beam shape result in variations in the proportion of columnar grains. The EBSD-derived percentages of columnar grains for circular, annular, square, and diamond-shaped beams are approximately 88%, 85%, 86%, and 95%, respectively. This observation demonstrates a satisfactory agreement between the numerically predicted grain morphologies following Hunt's model and the EBSD-derived measurements.

3.2. Melt-pool behaviour

Fig. 4 shows three snapshots of thermal and fluid flow fields over the melt-pool surface for circular beams with Gaussian and top-hat intensity profiles after reaching the quasi-steady-state condition. The results show that the molten metal flows from the melt-pool rim towards its central part because of the Marangoni shear force, which agrees with experimental observations of Mills et al. [46]. The molten metal temperature in the central part of the pool is above the critical temperature for which the value of the temperature gradient of surface tension ($\mathrm{d}\gamma/\mathrm{d}T$) is positive, resulting in an outward Marangoni flow from the central part towards the melt-pool rim. A complex unsteady flow pattern forms in the central part of the pool where the inward and the outward streams interact. Although the melt-pool resembles an almost symmetric shape with respect to the *y*-*z* plane, the molten metal flow and the temperature distribution in the pool are inherently unsteady and asymmetric due to hydrodynamic instabilities, requiring a transient and fully three-dimensional model to simulate transport phenomena in the pool properly. The thermal energy absorbed by the material diffuses through the material by conduction and advects with fluid flow in the pool. The overall energy transfer due to heat conduction and advection in combination with heat loss from the material determines the melt-pool shape; however, heat loss from the material due to radiation and convection is about 0.3% of the absorbed laser optical power, and thus its effect is negligible. Maximum fluid velocity in the pool is in the order of $\mathcal{O}(0.6\,\mathrm{m\,s^{-1}})$, resulting in a Péclet number ($\mathrm{Pe} = \rho c_p \mathscr{D} \|\mathbf{u}\|/k$) of about 100 that signifies the dominant effect of advection in total energy transfer.

For the process parameters studied here, the melt-pool dimensions obtained using circular beams with top-hat and Gaussian intensity profiles are comparable but the peak temperature obtained using a beam

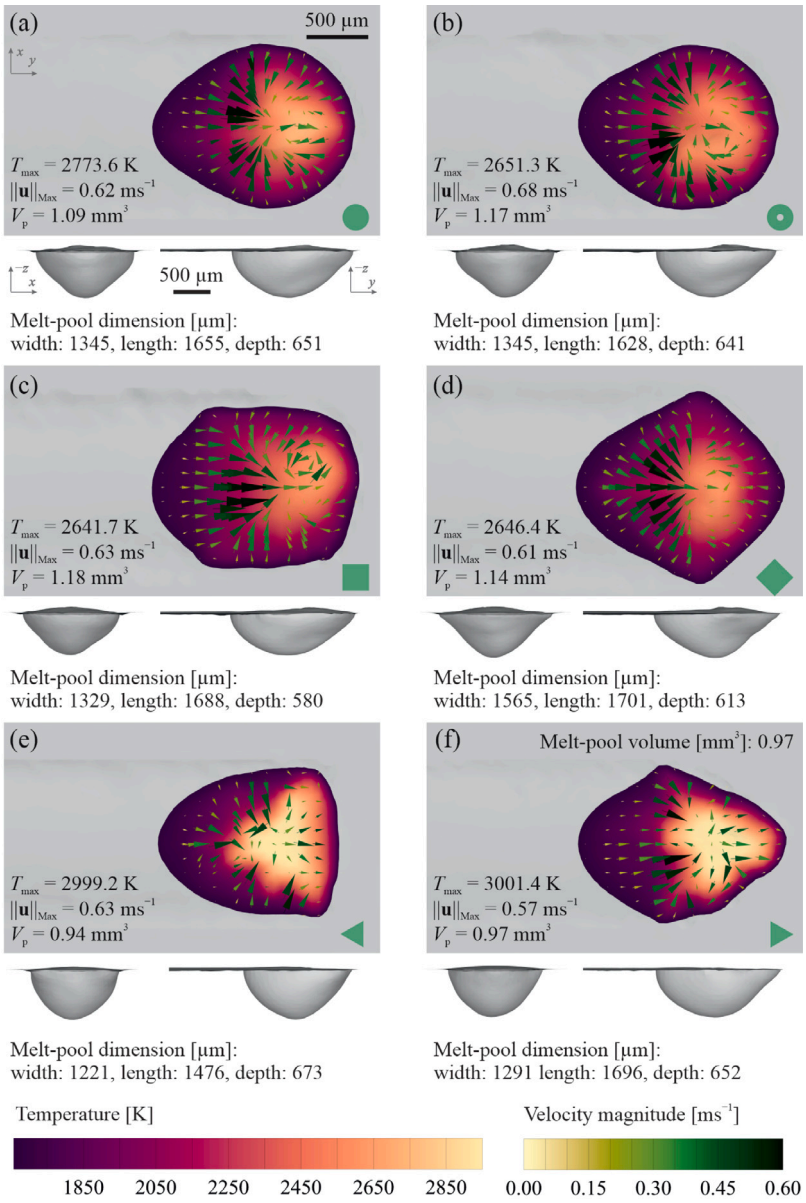

Fig. 5. Thermal and fluid flow fields over the melt-pool surface and the predicted melt-pool shapes for different laser beam shapes after reaching the quasi-steady-state condition (t = 0.65 s). The laser power is 700 W, the beam has a uniform intensity profile and the travel speed is 1.5×10^{-2} m s^{-1}. Green symbols on each subfigure show the laser beam shape. (For interpretation of the references to colour in this figure legend, the reader is referred to the web version of this article.)

with a Gaussian intensity profile is about 7% higher than that using a beam with a top-hat intensity profile. This is because the peak beam intensity of a Gaussian profile is higher than that of a top-hat profile for similar laser power and focal spot diameter. However, the intensity of the Gaussian beam rapidly reduces to values less than that of the top-hat beam when moving away from the pool centre. The greater peak temperature at the pool centre obtained using the Gaussian beam also results in higher absorptivity of laser energy that increases with temperature [13]. Accordingly, the magnitudes of temperature gradient and Marangoni shear force for the case with a Gaussian intensity profile are greater than those with a top-hat intensity profile, resulting in more sensitivity to spatial disturbances when using a beam with a Gaussian intensity profile. The maximum fluid velocity predicted for the case with a Gaussian intensity profile seems to be generally lower than that with a top-hat intensity profile, which is attributed to the greater outward Marangoni force in the former case.

Melt-pool behaviour in laser melting cannot be characterised solely based on laser power, spot size, travel speed and material properties; and information about beam shape and laser intensity profile is also required. Reshaping the laser beam can lead to changes in power density $\mathscr{P}_d$ and interaction time (t_i), the product of which results in energy density $\mathscr{E}_d$ [47] that critically affects the melt-pool behaviour [48]. Fig. 5 shows the numerically predicted temperature distribution and velocity vectors over the melt-pool surface and melt-pool shape for different laser beam shapes with uniform intensity profiles. For all the beam shapes studied here, an inward flow from the melt-pool rim is observed over the surface that collides with an outward flow close to the pool centre, the interaction of which leads to the formation of vortex flow over the surface that enhances fluid mixing in the pool. Although the total heat input to the material is almost identical for different beam shapes,[1] the predicted melt-pool dimensions

[1] The value of laser absorptivity depends on surface temperature, material composition and laser beam incidence angle [37]. Such effects are accounted for in the absorptivity model employed in the present numerical simulations.

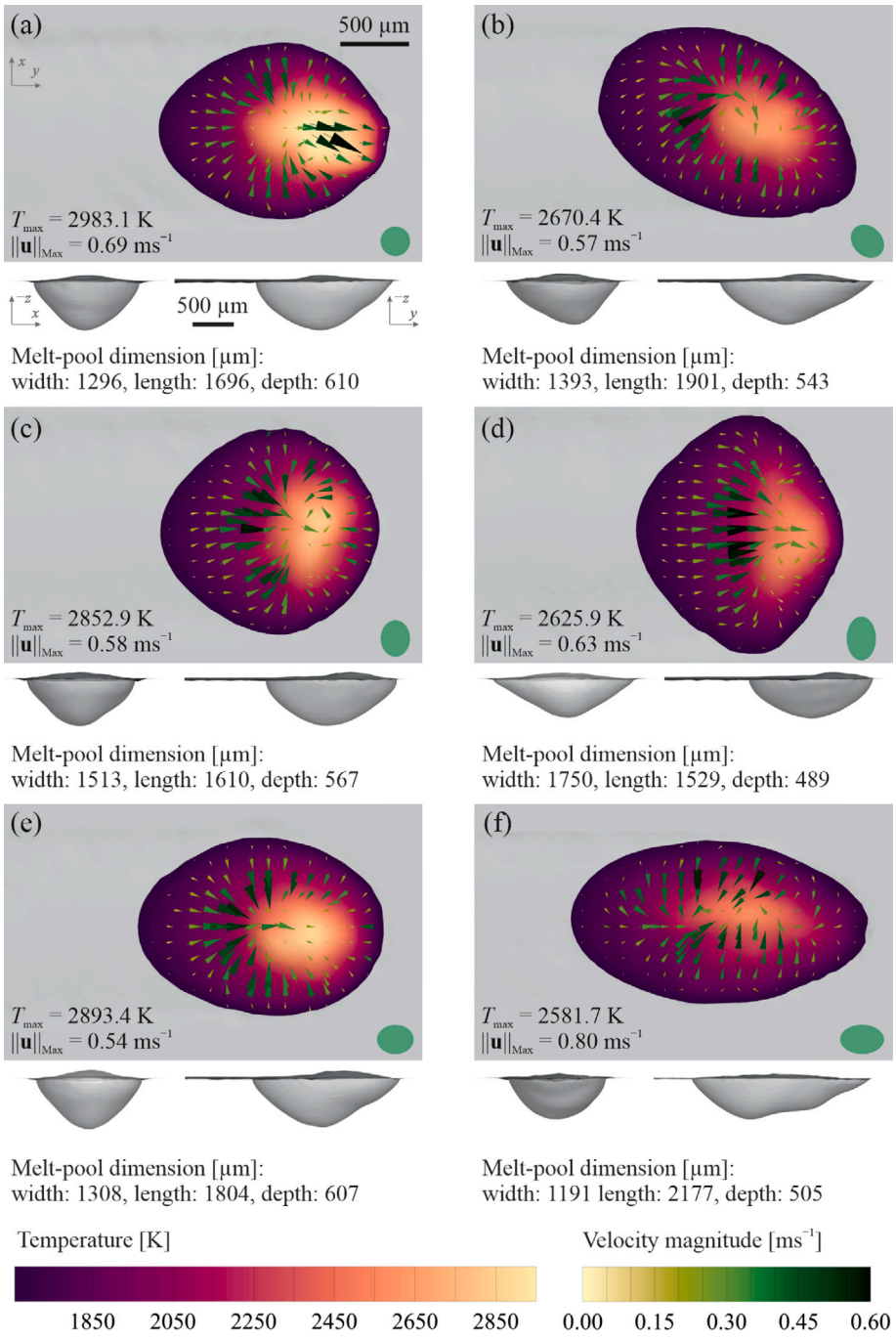

Fig. 6. The effects of laser beam incidence angle on thermal and fluid flow fields over the melt-pool surface and the pool shapes after reaching quasi-steady-state condition ($t = 0.65$ s). The laser beam is perpendicular to the x-y plane in subfigure a. Beam shape in subfigure b is produced by inclining the beam about both x and y axes by 45°. Beam shapes in subfigures c and d are produced by inclining the beam about the y-axis by 45° and 60° respectively. Similarly, beam shapes in subfigures e and f are produced by inclining the beam about the x-axis by 45° and 60° respectively. The laser power is 700 W, the beam has a (pseudo-)Gaussian intensity profile and the travel speed is 1.5×10^{-2} m s^{-1}. Green symbols on each subfigure show the laser beam shape. (For interpretation of the references to colour in this figure legend, the reader is referred to the web version of this article.)

differ considerably. The results show that there is not necessarily a one-to-one relationship between energy density and melt-pool volume, hence employing the concept of energy density is insufficient to explain changes in melt-pool dimensions obtained using different beam shapes. Assuming that the average laser absorptivity is similar for different beam shapes, it can be argued, based on the conservation of energy principle, that the material's total enthalpy must be identical when employing different beam shapes because the total heat input is the same. Therefore, variations in the thermal field should also be accounted for in addition to the energy density to explain the difference between melt-pool shapes obtained using different beam shapes. Changes in the pool shape also lead to changes in the direction and magnitude of temperature gradients, affecting the grain morphology of the material after solidification [49].

Elliptical beam shapes with different energy densities can be produced by changing the incidence angle of circular laser beams. A change in the laser beam incidence angle not only distorts the beam

Hence, the total energy input to the material is not necessarily the same for different cases studied in the present work.

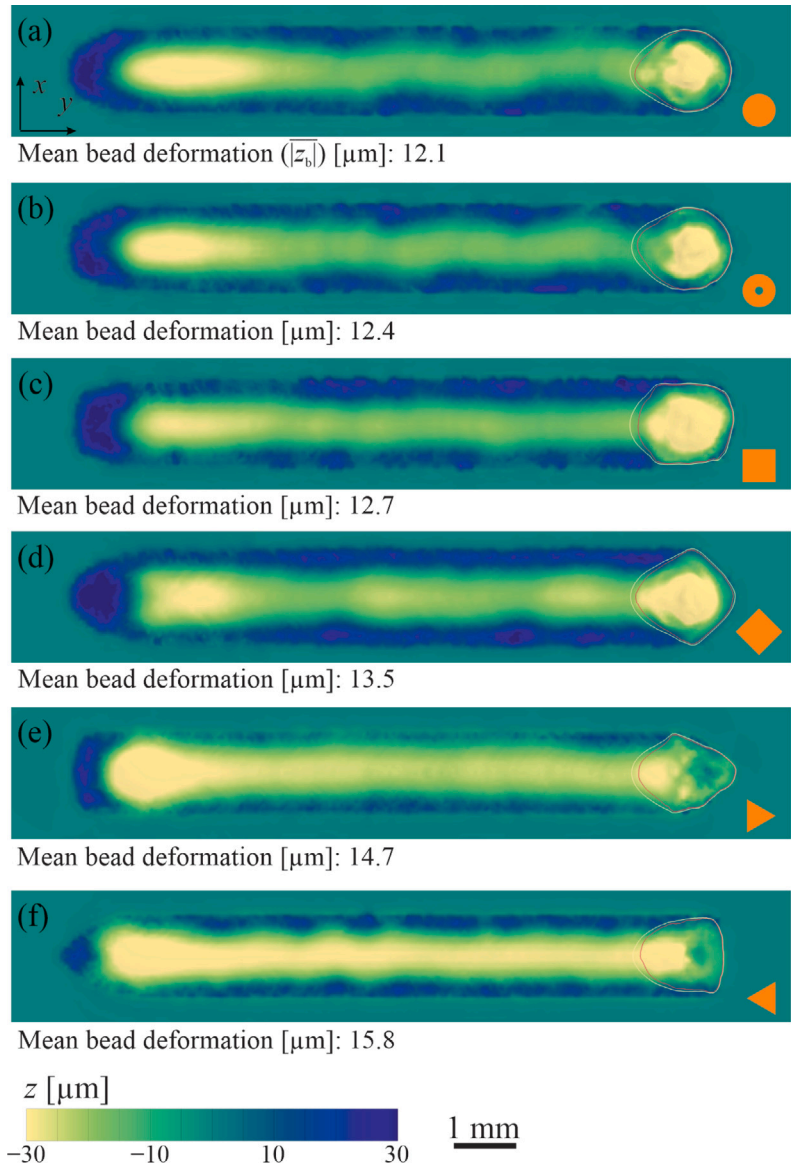

Fig. 7. Surface profile of the bead obtained from the numerical simulations for different laser beam shapes ($t = 0.65$ s). The laser power is 700 W, the beam has a uniform intensity profile and the travel speed is 1.5×10^{-2} m s^{-1}. Orange symbols on each subfigure show the laser beam shape. Negative values of z indicate surface elevation. Bead deformation values over the melt track, excluding the molten region, were employed to compute mean bead deformations. (For interpretation of the references to colour in this figure legend, the reader is referred to the web version of this article.)

shape but also affects the laser absorptivity and hence the total energy input to the material. Fig. 6 shows the numerically predicted temperature distribution and velocity vectors over the melt-pool surface and the pool shape for different laser beam incidence angles with (pseudo-)Gaussian intensity profiles. The flow pattern obtained using inclined beams seems similar to that obtained using the respective circular beam, and the molten metal flows from the melt-pool rim toward its centre. The melt-pool shape projected on the x-z plane resembles a symmetric shape for all the laser beam inclination angles except those where the beam is inclined about both x and y axes (see Fig. 6(b)). For the cases studied in the present work where an Yb:YAG laser with an emission wavelength of 1.030×10^{-6} m is employed, the average absorptivity of stainless steel AISI 316L increases by 2%–3% and 8%–12% by increasing the inclination angle from 0° to 45° and 60° respectively [13]. Although total energy input to the material increases by inclining the laser beam due to enhanced laser absorptivity, power density decreases with increasing the inclination angle because of the considerable increase in the spot area $\mathscr{A}$ (41.4% for an inclination angle of 45° and 99.4% for an inclination angle of 60°). When the laser spot is elongated in the transverse direction (*i.e.* inclining the beam about the y-axis), the interaction time remains the same as that of the circular beam; therefore, the overall effect of inclining the laser beam is a decrease in the energy density and thus the melt-pool depth and peak temperature. Similarly, the power density decreases when the spot is elongated in the scanning direction because of the increased spot area; however, decrease in the energy density is less than that of the case with a laser spot elongated in the transverse direction due to the increased interaction time. Hence, deeper melt-pools are observed when the beam is elongated in the scanning direction compared to those where the spot is elongated in the transverse direction. The present numerical results agree with the experimental observations reported in the literature [8,15,18,50] for conduction-mode laser melting.

3.3. Bead profile

Bead profile and surface quality after laser melting are influenced by the thermal and fluid flow fields in the melt-pool. Fig. 7 shows

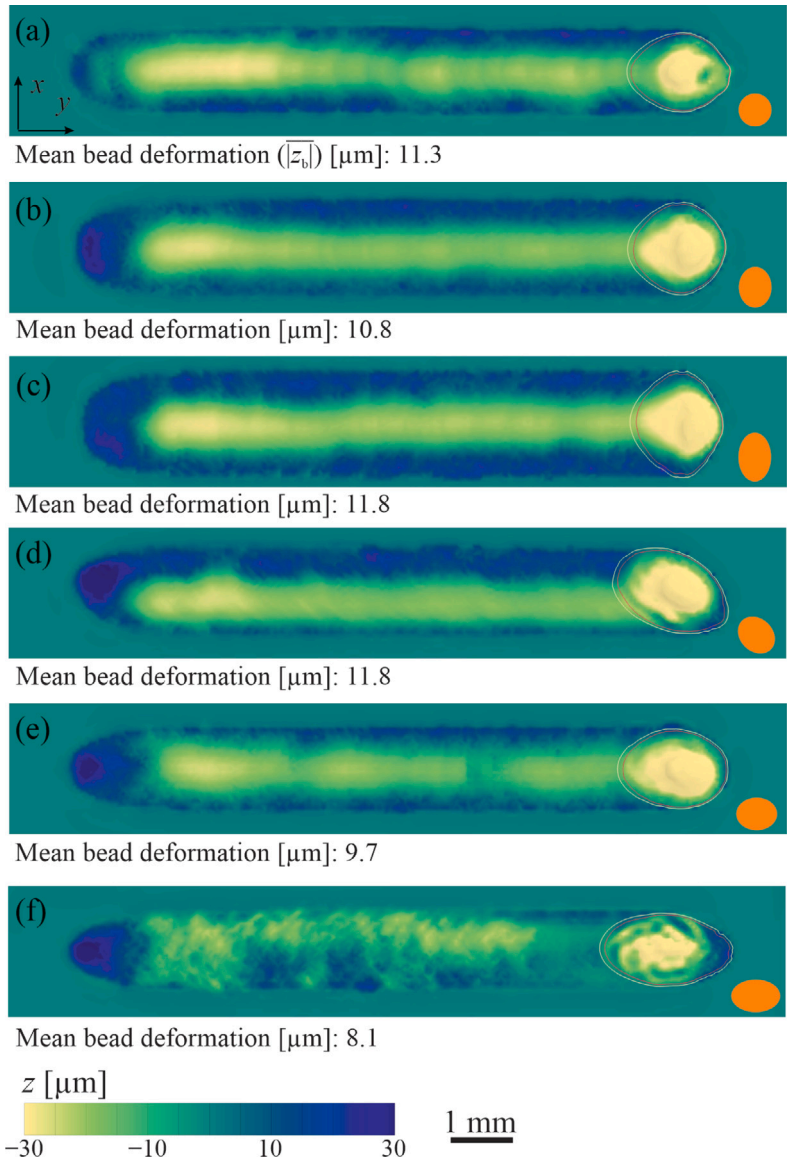

Fig. 8. Surface profile of the bead obtained from the numerical simulations for different laser beam incidence angles (t = 0.65 s). The laser power is 700 W, the beam has a (pseudo-)Gaussian intensity profile and the travel speed is 1.5×10^{-2} m s^{-1}. Orange symbols on each subfigure show the laser beam shape. Negative values of z indicate surface elevation. Bead deformation values over the melt track, excluding the molten region, were employed to compute mean bead deformations. (For interpretation of the references to colour in this figure legend, the reader is referred to the web version of this article.)

the surface profile of the bead measured in the z direction with reference to the un-melted surface and the arithmetic mean of the absolute bead deformation ($\overline{|z_b|}$) for different laser beam shapes with uniform intensity profiles. The bead surface is elevated in the central region of the melt track due to inward molten metal flow during laser melting for all the beam shapes shown in Fig. 7. Since the mass of the workpiece is almost unchanged during the process (*i.e.* vaporisation of the material and changes in the material density are negligible in conduction-mode laser melting), the bead surface is depressed in regions close to the outer boundaries of the track. The mean bead deformations obtained using circular, annular and square beam shapes appear to be similar and in the order of 12 μm that is lower than those obtained using diamond and triangular beam shapes, which can be attributed to the lower energy densities of the former cases. For some cases, the crest trail of the bead shows a wavy pattern that is due to molten metal flow instabilities during laser melting. Although no humping defect is observed for the cases studied in the present work, the surface profile obtained using the diamond beam shape (Fig. 7(d)) suggests that the bead could be prone to a humping defect.

Fig. 8 shows the surface profile of the bead for different laser beam shapes with (pseudo-)Gaussian intensity profiles. The bead surface produced using the circular beam with a Gaussian intensity profile shows solidified waves that result from pulsating molten metal flow instabilities [12,37,51]. Elongation of the laser spot in the transverse direction increases the bead width and seems to have an insignificant influence on the mean bead deformation. In contrast, elongation of the laser spot in the scanning direction does not change the bead width and reduces the mean bead deformation. The results indicate that inclining the beam about the y-axis by 60° (Fig. 8(f)) results in irregular surface deformations that can be ascribed to the flow instabilities in the melt pool. The bead profile obtained using a beam inclined about both x and y axes (Fig. 8(d)) differs from the other cases and is elevated in regions close to one edge of the melt track and is depressed in regions close to the other edge. The results show that the laser beam inclination

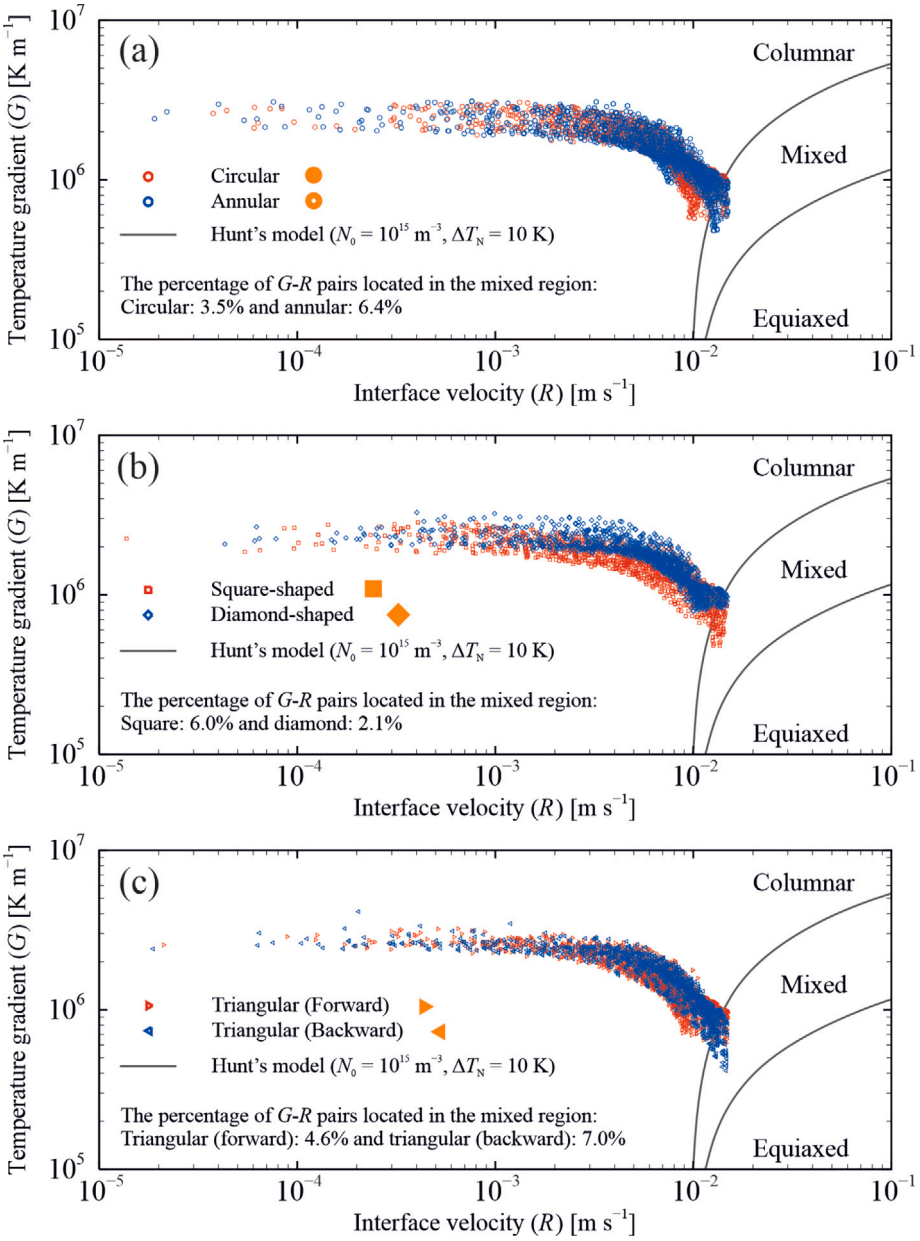

Fig. 9. Scatter plot of *G-R* data on the solidification map for different laser beam shapes with uniform intensity profiles after reaching quasi-steady-state condition ($t = 0.65$ s). The laser power is 700 W and the travel speed is 1.5×10^{-2} m s^{-1}. Orange symbols show the laser beam shape. (For interpretation of the references to colour in this figure legend, the reader is referred to the web version of this article.)

angle can be utilised as a potential means to control bead profile in laser melting processes.

3.4. Microstructural grain morphology

The present high-fidelity numerical predictions revealed that laser beam shaping significantly affects the melt-pool shape and thermal and fluid flow fields in conduction-mode laser melting. This can lead to changes in the material's microstructural grain structure and macroscopic properties after solidification. The distribution of *G-R* pairs on the solidification map are shown in Figs. 9 and 10 for different laser beam shapes and inclination angles respectively. The results suggest that changing the laser beam shape leads to the variation of the ratio of columnar to equiaxed grains. Since the travel speed was the same in all the simulations, the value of solidification growth rate R, which scales with the travel speed (see Eq. (6)), is similar for all the cases. However, the value of temperature gradient G ranges between 4×10^5 K m^{-1} and 7×10^6 K m^{-1} for different laser beam shapes and inclination angles studied in the present work. Due to the large magnitude of temperature gradients in conduction-mode laser melting ($\mathcal{O}(10^6)$ K), it is unlikely that equiaxed grains nucleate homogeneously during solidification [52, 53]. Grid points located at the melt-pool tail on the track centreline are the farthest points from the centroid of the laser spot and have the lowest temperature gradient G and the highest solidification growth rate R (*i.e.* the lowest G/R); hence, equiaxed and mixed columnar-equiaxed grains are more likely to form in that region. For partially penetrated melt-pools, the highest G/R values are found at the fusion boundary and close to the melt-pool bottom and sides since the solidification growth rate R is minimum at those locations; thus, non-equiaxed (*i.e.* planar, cellular and columnar) grains are expected to form in those regions [3].

The results presented in Fig. 9 indicate that changing the beam shape from circular shape leads to a decrease in the nucleation propensity of fully-columnar grains except for the diamond beam shape.

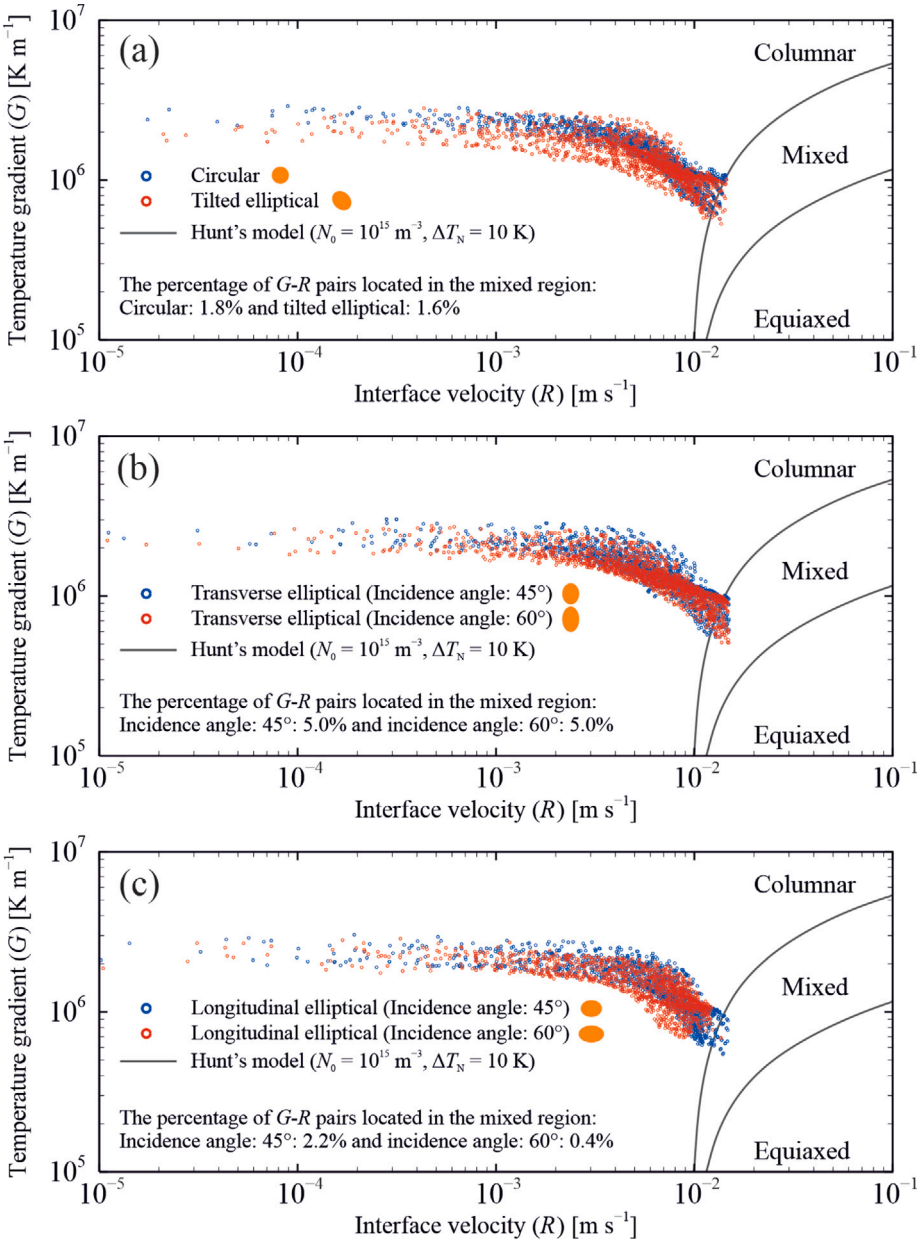

Fig. 10. Scatter plot of G-R data on the solidification map for different laser beam inclination angles with Gaussian intensity profiles after reaching quasi-steady-state condition ($t = 0.65$ s). The laser power is 700 W and the travel speed is 1.5×10^{-2} m s^{-1}. Orange symbols show the laser beam shape. (For interpretation of the references to colour in this figure legend, the reader is referred to the web version of this article.)

Calculating the percentage of G-R pairs located in the mixed columnar-equiaxed region for different laser beam shapes, it is found that employing backward triangular (7.0%), annular (6.4%) and square (6.0%) beam shapes results in the highest nucleation propensity of equiaxed grains. The distribution of G-R pairs in Fig. 10 indicate that elongation of the laser spot in the transverse direction decreases the nucleation propensity of fully-columnar grains that can be ascribed to the decrease in the magnitude of temperature gradient G at the melt-pool tail. Elongation of laser spot in the scanning direction by inclining the beam by 45° seems to have insignificant effect on the nucleation propensity of fully-columnar grains; however further increase in the inclination angle to 60° leads to an increase in the nucleation propensity of fully-columnar grains. This is because melt-pool elongation in the scanning direction results in an increase in the average angle between the maximum heat flow direction and the scanning direction (α), leading to a decrease in the solidification growth rate (R) and an increase in the value of G/R.

4. Conclusions

The effects of laser beam shaping on melt-pool behaviour, solidified bead profile and microstructural gain morphology were studied comprehensively through high-fidelity numerical experiments for conduction-mode laser melting of stainless steel AISI 316L. Three-dimensional unsteady numerical simulations were performed to examine the effects of laser beam intensity profile, shape and inclination angle on the melt-pool behaviour. Critical physical phenomena in laser melting such as temporal and spatial variations of absorptivity, heat and fluid flow dynamics, solidification and melting, and free-surface oscillations were accounted for in the present computational model. Moreover, experiments were performed using different laser beam shapes and the validity of the present numerical predictions was demonstrated. Based on the results of the present work, the following conclusions are drawn.

- Altering the laser intensity profile leads to changes in the thermal and fluid flow fields in the melt pool, which in turn affect the melt-pool dimensions, melt-track bead profile and grain morphology. Moreover, the sensitivity of melt-pool responses to spatial and temporal disturbances, and hence process stability, depend on the laser-intensity profile.
- For identical processing parameters, reshaping the laser beam can change the energy density that affects the melt-pool behaviour. However, variations in the melt-pool shape and volume caused by laser beam shaping cannot be described solely based on the concept of energy density, and the material's total enthalpy should be taken into consideration.
- Inclining the laser beam not only distorts the beam shape but also affects the laser absorptivity and hence total energy input to the material. However, the increase in the absorptivity due to laser beam inclination is considerably less than the increase in the spot area; thus, the overall effect of laser beam inclination is a reduction in the power density. Employing identical processing parameters and inclination angles, a deeper melt-pool was observed when the laser spot was elongated in the scanning direction compared to the case in which the spot was elongated in the transverse direction, which can be ascribed to the increased interaction time in the former case.
- Laser beam shaping has a notable effect on melt-track bead profile and can be utilised as a potential means to control bead profile in laser welding and additive manufacturing.
- Laser beam shaping significantly affects microstructural grain morphology by influencing the thermal gradient and solidification growth rate. The present findings demonstrate that the material's microstructure, and thus its macroscopic properties, can be adjusted locally through laser beam shaping.

The findings of the present work provide an improved insight into the effects of laser beam shaping in laser welding and additive manufacturing. The simulation-based approach developed in the present work offers new routes for design space exploration and process optimisation.

Future research in this area could focus on advancing the optimisation of laser beam shaping for laser-based additive manufacturing. One promising avenue is to explore multi-objective optimisation techniques that consider not only the melt-pool behaviour and bead profile but also the microstructural grain morphology. This would enable the development of tailor-made microstructures with desired properties for specific applications. Data-driven approaches, combining experimental data with numerical simulations, could be employed to create predictive models that guide the selection of optimal laser beam intensity profiles for achieving precise control over microstructural characteristics. Additionally, investigating the influence of various process parameters and materials on the interaction between laser beam shaping and microstructure could open new avenues for tailoring material properties in additive manufacturing, enhancing the design and performance of additively manufactured components.

CRediT authorship contribution statement

Amin Ebrahimi: Conceptualisation, Methodology, Software, Validation, Formal analysis, Investigation, Resources, Data curation, Writing – original draft, Writing – review & editing, Visualisation, Project administration. **Mohammad Sattari:** Validation, Writing – review & editing. **Aravind Babu:** Validation, Writing – review & editing. **Arjun Sood:** Validation. **Gert-Willem R.B.E. Römer:** Resources, Writing – review & editing, Funding acquisition. **Marcel J.M. Hermans:** Resources, Writing – review & editing, Project administration, Funding acquisition.

Declaration of competing interest

The authors declare that they have no known competing financial interests or personal relationships that could have appeared to influence the work reported in this paper.

Data availability

The raw/processed data required to reproduce these findings cannot be shared at this time due to their large size, but representative samples of the research data are presented in the paper. Other datasets generated during this study are available from the corresponding author on reasonable request.

Acknowledgements

This research was carried out under project number S17024 in the framework of the Partnership Program of the Materials innovation institute M2i, The Netherlands (www.m2i.nl) and the Netherlands Organisation for Scientific Research, The Netherlands (www.nwo.nl). This research project is part of the AiM2XL program (www.m2i.nl/aim2xl).

References

[1] Herzog D, Seyda V, Wycisk E, Emmelmann C. Additive manufacturing of metals. Acta Mater 2016;117:371–92. http://dx.doi.org/10.1016/j.actamat.2016.07.019.

[2] Khare J, Kaul R, Ganesh P, Kumar H, Jagdheesh R, Nath AK. Laser beam shaping for microstructural control during laser surface melting. J Laser Appl 2007;19(1):1–7. http://dx.doi.org/10.2351/1.2402522.

[3] Roehling TT, Wu SS, Khairallah SA, Roehling JD, Soezeri SS, Crumb MF, et al. Modulating laser intensity profile ellipticity for microstructural control during metal additive manufacturing. Acta Mater 2017;128:197–206. http://dx.doi.org/10.1016/j.actamat.2017.02.025.

[4] Roehling TT, Shi R, Khairallah SA, Roehling JD, Guss GM, McKeown JT, et al. Controlling grain nucleation and morphology by laser beam shaping in metal additive manufacturing. Mater Des 2020;195:109071. http://dx.doi.org/10.1016/j.matdes.2020.109071.

[5] Shi R, Khairallah SA, Roehling TT, Heo TW, McKeown JT, Matthews MJ. Microstructural control in metal laser powder bed fusion additive manufacturing using laser beam shaping strategy. Acta Mater 2020;184:284–305. http://dx.doi.org/10.1016/j.actamat.2019.11.053.

[6] Mei L, Yan D, Chen G, Wang Z, Chen S. Influence of laser beam incidence angle on laser lap welding quality of galvanized steels. Opt Commun 2017;402:147–58. http://dx.doi.org/10.1016/j.optcom.2017.05.032.

[7] Grünewald J, Gehringer F, Schmöller M, Wudy K. Influence of ring-shaped beam profiles on process stability and productivity in laser-based powder bed fusion of AISI ?316L. Metals 2021;11(12):1989. http://dx.doi.org/10.3390/met11121989.

[8] Fathi-Hafshejani P, Soltani-Tehrani A, Shamsaei N, Mahjouri-Samani M. Laser incidence angle influence on energy density variations, surface roughness, and porosity of additively manufactured parts. Addit Manuf 2022;50:102572. http://dx.doi.org/10.1016/j.addma.2021.102572.

[9] Ebrahimi A, Kleijn CR, Richardson IM. A simulation-based approach to characterise melt-pool oscillations during gas tungsten arc welding. Int J Heat Mass Transfer 2021;164:120535a. http://dx.doi.org/10.1016/j.ijheatmasstransfer.2020.120535.

[10] Ebrahimi A, Kleijn CR, Hermans MJM, Richardson IM. The effects of process parameters on melt-pool oscillatory behaviour in gas tungsten arc welding. J Phys D: Appl Phys 2021;54(27):275303b. http://dx.doi.org/10.1088/1361-6463/abf808.

[11] Cooke S, Ahmadi K, Willerth S, Herring R. Metal additive manufacturing: Technology, metallurgy and modelling. J Manuf Processes 2020;57:978–1003. http://dx.doi.org/10.1016/j.jmapro.2020.07.025.

[12] Ebrahimi A, Kleijn CR, Richardson IM. Numerical study of molten metal melt pool behaviour during conduction-mode laser spot melting. J Phys D: Appl Phys 2021;54:105304c. http://dx.doi.org/10.1088/1361-6463/abca62.

[13] Ebrahimi A, Sattari M, Bremer SJL, Luckabauer M, willem R.B.E. Römer G, Richardson IM, et al. The influence of laser characteristics on internal flow behaviour in laser melting of metallic substrates. Mater Des 2022;214:110385. http://dx.doi.org/10.1016/j.matdes.2022.110385.

[14] Ebrahimi A, Hermans MJ. Laser butt welding of thin stainless steel 316L sheets in asymmetric configurations: A numerical study. J Adv Join Processes 2023;8:100154. http://dx.doi.org/10.1016/j.jajp.2023.100154.

[15] Ayoola WA, Suder WJ, Williams SW. Effect of beam shape and spatial energy distribution on weld bead geometry in conduction welding. Opt Laser Technol 2019;117:280–7. http://dx.doi.org/10.1016/j.optlastec.2019.04.025.

[16] Tenbrock C, Fischer FG, Wissenbach K, Schleifenbaum JH, Wagenblast P, Meiners W, et al. Influence of keyhole and conduction mode melting for top-hat shaped beam profiles in laser powder bed fusion. J Mater Process Technol 2020;278:116514. http://dx.doi.org/10.1016/j.jmatprotec.2019.116514.

[17] Tumkur TU, Voisin T, Shi R, Depond PJ, Roehling TT, Wu S, et al. Nondiffractive beam shaping for enhanced optothermal control in metal additive manufacturing. Sci Adv 2021;7(38). http://dx.doi.org/10.1126/sciadv.abg9358.

[18] Mi Y, Mahade S, Sikström F, Choquet I, Joshi S, Ancona A. Conduction mode laser welding with beam shaping using a deformable mirror. Opt Laser Technol 2022;148:107718. http://dx.doi.org/10.1016/j.optlastec.2021.107718.
[19] Pamarthi VV, Sun T, Das A, Franciosa P. Tailoring the weld microstructure to prevent solidification cracking in remote laser welding of AA6005 aluminium alloys using adjustable ringmode beam. J Mater Res Technol 2023;25:7154–68. http://dx.doi.org/10.1016/j.jmrt.2023.07.154.
[20] Cloots M, Uggowitzer PJ, Wegener K. Investigations on the microstructure and crack formation of IN738LC samples processed by selective laser melting using Gaussian and doughnut profiles. Mater Des 2016;89:770–84. http://dx.doi.org/10.1016/j.matdes.2015.10.027.
[21] Kubiak M, Piekarska W, Stano S. Modelling of laser beam heat source based on experimental research of Yb:YAG laser power distribution. Int J Heat Mass Transfer 2015;83:679–89. http://dx.doi.org/10.1016/j.ijheatmasstransfer.2014.12.052.
[22] Collins PC, Brice D, Samimi P, Ghamarian I, Fraser H. Microstructural control of additively manufactured metallic materials. Annu Rev Mater Res 2016;46(1):63–91. http://dx.doi.org/10.1146/annurev-matsci-070115-031816.
[23] Bremer SJ, Luckabauer M, willem R.B.E. Römer G. Laser intensity profile as a means to steer microstructure of deposited tracks in Directed Energy Deposition. Mater Des 2023;227:111725. http://dx.doi.org/10.1016/j.matdes.2023.111725.
[24] Dickey FM, Holswade SC, Shealy DL, editors. Laser beam shaping applications. CRC Press; 2018, http://dx.doi.org/10.1201/9781420028065.
[25] Salter PS, Booth MJ. Adaptive optics in laser processing. Light: Sci Appl 2019;8(1). http://dx.doi.org/10.1038/s41377-019-0215-1.
[26] Bi J, Wu L, Li S, Yang Z, Jia X, Starostenkov MD, et al. Beam shaping technology and its application in metal laser additive manufacturing: A review. J Mater Res Technol 2023;26:4606–28. http://dx.doi.org/10.1016/j.jmrt.2023.08.037.
[27] Sundqvist J, Kaplan AFH, Shachaf L, Brodsky A, Kong C, Blackburn J, et al. Numerical optimization approaches of single-pulse conduction laser welding by beam shape tailoring. Opt Lasers Eng 2016;79:48–54. http://dx.doi.org/10.1016/j.optlaseng.2015.12.001.
[28] Kell J, Tyrer JR, Higginson RL, Jones JC, Noden S. Laser weld pool management through diffractive holographic optics. Mater Sci Technol 2012;28(3):354–63. http://dx.doi.org/10.1179/1743284711y.0000000050.
[29] Funck K, Nett R, Ostendorf A. Tailored beam shaping for laser spot joining of highly conductive thin foils. Physics Procedia 2014;56:750–8. http://dx.doi.org/10.1016/j.phpro.2014.08.082.
[30] Han L, Liou FW. Numerical investigation of the influence of laser beam mode on melt pool. Int J Heat Mass Transfer 2004;47(19–20):4385–402. http://dx.doi.org/10.1016/j.ijheatmasstransfer.2004.04.036.
[31] Safdar S, Li L, Sheikh MA. Numerical analysis of the effects of non-conventional laser beam geometries during laser melting of metallic materials. J Phys D: Appl Phys 2007;40(2):593–603. http://dx.doi.org/10.1088/0022-3727/40/2/039.
[32] Rasch M, Roider C, Kohl S, Strauß J, Maurer N, Nagulin KY, et al. Shaped laser beam profiles for heat conduction welding of aluminium-copper alloys. Opt Lasers Eng 2019;115:179–89. http://dx.doi.org/10.1016/j.optlaseng.2018.11.025.
[33] Abadi SMANR, Mi Y, Sikström F, Ancona A, Choquet I. Effect of shaped laser beam profiles on melt flow dynamics in conduction mode welding. Int J Therm Sci 2021;166:106957. http://dx.doi.org/10.1016/j.ijthermalsci.2021.106957.
[34] Release 19.2. ANSYS fluent. https://www.ansys.com/.
[35] Hirt CW, Nichols BD. Volume of fluid (VOF) method for the dynamics of free boundaries. J Comput Phys 1981;39(1):201–25. http://dx.doi.org/10.1016/0021-9991(81)90145-5.
[36] Ebrahimi A, Kleijn CR, Richardson IM. The influence of surface deformation on thermocapillary flow instabilities in low Prandtl melting pools with surfactants. In: Proceedings of the 5th world congress on mechanical, chemical, and material engineering. Avestia Publishing; 2019, http://dx.doi.org/10.11159/htff19.201.
[37] Ebrahimi A. Molten metal oscillatory behaviour in advanced fusion-based manufacturing processes (PhD Dissertation), The Netherlands: Delft University of Technology, Delft; 2022.
[38] Ebrahimi A, Kleijn CR, Richardson IM. Sensitivity of numerical predictions to the permeability coefficient in simulations of melting and solidification using the enthalpy-porosity method. Energies 2019;12(22):4360b. http://dx.doi.org/10.3390/en12224360.
[39] Ubbink O. Numerical prediction of two fluid systems with sharp interfaces (PhD Dissertation), London, United Kingdom: Imperial College London (University of London); 1997, http://hdl.handle.net/10044/1/8604.
[40] Issa RI. Solution of the implicitly discretised fluid flow equations by operator-splitting. J Comput Phys 1986;62(1):40–65. http://dx.doi.org/10.1016/0021-9991(86)90099-9.
[41] Patankar SV. Numerical heat transfer and fluid flow. 1st edition. Taylor & Francis Inc; 1980.
[42] Hunt JD. Steady state columnar and equiaxed growth of dendrites and eutectic. Mater Sci Eng 1984;65(1):75–83. http://dx.doi.org/10.1016/0025-5416(84)90201-5.
[43] Knapp GL, Raghavan N, Plotkowski A, DebRoy T. Experiments and simulations on solidification microstructure for Inconel 718 in powder bed fusion electron beam additive manufacturing. Addit Manuf 2019;25:511–21. http://dx.doi.org/10.1016/j.addma.2018.12.001.
[44] Gäumann M, Bezençon C, Canalis P, Kurz W. Single-crystal laser deposition of superalloys: processing–microstructure maps. Acta Mater 2001;49(6):1051–62. http://dx.doi.org/10.1016/s1359-6454(00)00367-0.
[45] Tan W, Shin YC. Multi-scale modeling of solidification and microstructure development in laser keyhole welding process for austenitic stainless steel. Comput Mater Sci 2015;98:446–58. http://dx.doi.org/10.1016/j.commatsci.2014.10.063.
[46] Mills KC, Keene BJ, Brooks RF, Shirali A. Marangoni effects in welding. Phil Trans R Soc A 1998;356(1739):911–25. http://dx.doi.org/10.1098/rsta.1998.0196.
[47] Steen WM, Mazumder J. Laser material processing. London: Springer; 2010, http://dx.doi.org/10.1007/978-1-84996-062-5.
[48] Assuncao E, Williams S, Yapp D. Interaction time and beam diameter effects on the conduction mode limit. Opt Lasers Eng 2012;50(6):823–8. http://dx.doi.org/10.1016/j.optlaseng.2012.02.001.
[49] Rappaz M. Modelling of microstructure formation in solidification processes. Int Mater Rev 1989;34(1):93–124. http://dx.doi.org/10.1179/imr.1989.34.1.93.
[50] Liao Y-C, Yu M-H. Effects of laser beam energy and incident angle on the pulse laser welding of stainless steel thin sheet. J Mater Process Technol 2007;190(1):102–8. http://dx.doi.org/10.1016/j.jmatprotec.2007.03.102.
[51] Kidess A, Kenjereš S, Kleijn CR. The influence of surfactants on thermocapillary flow instabilities in low Prandtl melting pools. Phys Fluids 2016;28(6):062106. http://dx.doi.org/10.1063/1.4953797.
[52] Kurz W, Bezençon C, Gäumann M. Columnar to equiaxed transition in solidification processing. Sci Technol Adv Mater 2001;2(1):185–91. http://dx.doi.org/10.1016/s1468-6996(01)00047-x.
[53] He Y, Zhong M, Jones N, Beuth J, Webler B. The columnar-to-equiaxed transition in melt pools during laser powder bed fusion of M2 steel. Metall Mater Trans A 2021;52(9):4206–21. http://dx.doi.org/10.1007/s11661-021-06380-9.